Chai *et al. BMC Cancer* (2025) 25:907
https://doi.org/10.1186/s12885-025-14301-x

BMC Cancer

RESEARCH **Open Access**

Synthesizing [^{18}F]PSMA-1007 PET bone images from CT images with GAN for early detection of prostate cancer bone metastases: a pilot validation study

Liming Chai[1*], Xiaolong Yao[1], Xiaofeng Yang[1], Renhua Na[1], Wei Yan[1], Mingzheng Jiang[1], Haixu Zhu[1], Canwen Sun[1], Zeqiang Dai[1] and Xueying Yang[1]

Abstract

Background [^{18}F]FDG PET/CT scan combined with [^{18}F]PSMA-1007 PET/CT scan is commonly conducted for detecting bone metastases in prostate cancer (PCa). However, it is expensive and may expose patients to more radiation hazards. This study explores deep learning (DL) techniques to synthesize [^{18}F]PSMA-1007 PET bone images from CT bone images for the early detection of bone metastases in PCa, which may reduce additional PET/CT scans and relieve the burden on patients.

Methods We retrospectively collected paired whole-body (WB) [^{18}F]PSMA-1007 PET/CT images from 152 patients with clinical and pathological diagnosis results, including 123 PCa and 29 cases of benign lesions. The average age of the patients was 67.48 ± 10.87 years, and the average lesion size was 8.76 ± 15.5 mm. The paired low-dose CT and PET images were preprocessed and segmented to construct the WB bone structure images. 152 subjects were randomly stratified into training, validation, and test groups in the number of 92:41:19. Two generative adversarial network (GAN) models—Pix2pix and Cycle GAN—were trained to synthesize [^{18}F]PSMA-1007 PET bone images from paired CT bone images. The performance of two synthesis models was evaluated using quantitative metrics of mean absolute error (MAE), mean squared error (MSE), peak signal-to-noise ratio (PSNR), and structural similarity index metrics (SSIM), as well as the target-to-background ratio (TBR).

Results The results of DL-based image synthesis indicated that the synthesis of [^{18}F]PSMA-1007 PET bone images from low-dose CT bone images was highly feasible. The Pix2pix model performed better with an SSIM of 0.97, PSNR of 44.96, MSE of 0.80, and MAE of 0.10, respectively. The TBRs of bone metastasis lesions calculated on DL-synthesized PET bone images were highly correlated with those of real PET bone images (Pearson's $r > 0.90$) and had no significant differences ($p < 0.05$).

Conclusions It is feasible to generate synthetic [^{18}F]PSMA-1007 PET bone images from CT bone images by using DL techniques with reasonable accuracy, which can provide information for early detection of PCa bone metastases.

Keywords Prostate cancer, Bone metastases, [^{18}F]PSMA-1007, PET/CT, Image synthesis, Deep learning

Introduction

PCa is the most prevalent malignant tumor and a leading cause of oncological mortality in men [1]. Bone is the most common metastasis site of PCa, accounting

---

*Correspondence:
Liming Chai
chailm@126.com
[1] Department of Nuclear Medicine, People's Hospital of Xinjiang Uygur Autonomous Region, Urumqi 830001, China

for 88.7% of all PCa metastasis sites. About 85% to 100% of patients who die from PCa have bone metastases [2]. The clinical detection of bone metastases in PCa is crucial, as it can precipitate skeletal-related events (SREs), including pathological fractures, spinal cord compression, bone surgery, and bone radiation therapy, which can severely affect patients' quality of life and survival. Early detection and diagnosis of bone metastases in PCa are critical for improving patient outcomes, as they enable timely interventions to slow disease progression and reduce complications.

In clinical practice, technetium-99 m methyl diphosphonate ([$^{99\,m}$Tc]MDP) WB bone scan is the most common and cost-effective method for the early screening of PCa bone metastases. However, it has relatively low specificity in diagnosing bone metastases, and the intrinsic low resolution of nuclear medicine scintigraphy often leads to the omission of small lesions [2, 3]. Fluorine-18-Fludeoxyglucose ([^{18}F]FDG) is the most widely used radiotracer, and [^{18}F]FDG PET/CT imaging is effective for the diagnosis and staging of PCa, which has been demonstrated superior to [$^{99\,m}$Tc]MDP SPECT for detecting PCa bone metastasis [2, 3] . However, [^{18}F]FDG PET/CT is more sensitive in detecting osteolytic bone metastases, but has limited effectiveness in detecting osteoblastic lesions, which are predominant in PCa bone metastases [2, 3]. The accurate diagnosis of PCa bone metastases remains a significant clinical challenge.

Prostate-specific membrane antigen (PSMA) is a glycoprotein involved in PCa [4, 5]. Fluorine-18 PSMA ([^{18}F]PSMA)-1007 is a novel PSMA-based radiopharmaceutical and has rapidly become a popular method for PCa examination in recent years [4–7]. It is valuable for diagnostic evaluation, staging, risk stratification, detection of biochemical recurrence, and assessment of treatment efficacy in PCa due to its notable advantages, including a longer radiotracer half-life, a better PET image resolution, and predominant excretion via the hepatobiliary rather than urinary system [4–7]. [^{18}F]PSMA-1007 has distinct advantages in detecting primary prostate lesions, pelvic lymph node metastasis, and bone metastases, and shows superior to [^{18}F]FDG. However, its uptake in the liver, spleen, and intestines can affect the detection of metastasis in other regions, and uptaking in benign lesions is considerably higher [6, 7]. Additionally, the [^{18}F]PSMA-1007 PET/CT scan is more expensive. Therefore, in clinical practice, both [^{18}F]FDG and [^{18}F]PSMA-1007 PET/CT imaging may have complementary effects, and their combined use can provide a more comprehensive assessment of PCa bone metastasis. However, dual PET/CT scans increase the burden on both patients and the healthcare system.

To address challenges such as scanning radiation and the high cost of scans, medical image synthesis inter- and intra-modalities has gained increasing traction in clinical applications. With the rapid development of machine learning (ML) and DL in recent decades, DL-based image synthesis technology has become mainstream and shown great potential in the clinical workflow [8]. Salehjahromi et al. testified to the feasibility of applying DL (conditional GAN, cGAN) to obtain high-fidelity PET translated from CT [9]. The authors demonstrated synthetic PET' promising diagnostic values in lung cancer staging, early detection, and prognostication. Sanaat et al. proposed a DL model for generating the [^{18}F]FDG from early-phase Fluorine-18 Florbetapir ([^{18}F]FBP) and Fluorine-18 Flutemetamol ([^{18}F]FMM) PET images [10], through which the authors proposed an alternative to reduce the number of PET scans for multiple radiotracer scanning in research and clinical settings.

In hybrid PET/CT, CT image depicts anatomical and structural changes of bone with a high spatial resolution, thus the incorporation of both components of PET and CT enhances the evaluation accuracy of bone metastases [11]. This study hypothesizes that DL can generate synthetic [^{18}F]-PSMA-1007 PET WB bone structure images from CT scans. These synthetic images could offer valuable insights into bone metabolism and enhance clinical decision-making by aiding in the early detection of PCa bone metastases. To test this, we developed two GAN models—Pix2pix GAN and Cycle GAN—to perform this cross-modality CT-to-PET translation. We then evaluated the quality and clinical values of the synthetic PET bone structure images for PCa bone metastases diagnosis.

Materials and methods

Participants

In this retrospective study, we collected paired [^{18}F]PSMA-1007 PET/CT images from 152 patients of the People's Hospital of Xinjiang Uygur Autonomous Region from July 2022 to May 2023. All patients had clinical and pathological diagnoses, with 123 cases of PCa and 29 cases of benign lesions. The average age of the patients was 67.48 ± 10.87 years and the lesions were 8.76 ± 15.5 mm in size. Among those 123 PCa patients, 122 patients were staged N, and 77 patients staged M based on clinical TNM staging per diagnostic and treatment standards.

This study was approved by the Ethics Committee of the People's Hospital of Xinjiang Uygur Autonomous Region, China. Written informed consent was obtained from all patients.

PET/CT data acquisition

All 152 patients underwent [^{18}F]PSMA-1007 WB PET/CT scans using a Siemens Biograph mCT64 (Siemens Healthcare, Germany). The ^{18}F isotope was produced by GE Minitrace medical cyclotron, and the PSMA-1007 ligand was supplied by ABX company in Germany. The radiochemical purity of [^{18}F]PSMA-1007 exceeded 99%. [^{18}F]PSMA-1007 was injected into the patient's elbow vein 60 min before the examination at a dose of 7–10 mCi (2MBq/kg). Following the injection, patients were instructed to rest, drink plenty of water, and urinate more. Subsequently, the PET/CT scan was performed. The scanning range extended from the top of the head to the base of the thighs. The low-dose CT scan utilized an automatic milliampere second setting at 120 kV voltage, a 512 ×512 matrix, and a 5 mm thickness. The PET scan consisted of 5 to 6 beds, with each bed scanned for 2–3 min. PET images were reconstructed using the TrueX + TOF (ultra-HD PET) algorithm with 3 iterations and 21 subsets.

PET/CT data preprocessing, segmentation, and bone structure extraction

First, WB PET/CT data were preprocessed as follows. All CT images were stripped of the scanning table using Remove CT table module of 3D Slicer tool (version 5.2.2). All PET images were converted to standardized uptake values (SUV) and were co-registered with their paired CT images using the Elastix registration module of 3D Slicer [12].

Next, unlike most other studies that usually synthesize whole images [8–10], this study only tried to synthesize the bone tissue structure to investigate PCa bone metastases. In order to achieve this, the CT images were automatically segmented into 104 anatomical structures (27 organs, 59 bones, 10 muscles, and 8 vessels) by utilizing the TotalSegmentor module of 3D Slicer [13], from which we obtained the WB CT bone tissue structure segments. All WB CT bone tissue structure segments were reviewed by an experienced radiologist and corrected if needed. As such, CT bone tissue structure images and masks were obtained for all subjects.

Subsequently, the WB PET bone structures were segmented on the WB PET images by applying the WB CT bone tissue structure masks, which served as the ground truth for DL modeling later. In addition, the WB CT bone tissue structure images were transformed into X-ray attenuation coefficient maps [14], whose values ranged from 0 to 1, to serve as the input images for training DL models.

Last, in order to measure the TBR, the malignant bone metastasis lesions regions of interest (ROIs) and contralateral normal ROIs were delineated manually on the PET bone images by an experienced radiologist using 3D Slicer (Fig. 1).

GAN models development

All 152 subjects were randomly stratified into training, validation, and test groups in the number of 92:41:19 respectively. The DL training platform used the Medical Open Network for Artificial Intelligence (MONAI) (core version 1.1.0). The training environment were Windows 11 and Nvidia 16GB GPU. Two GAN models—Pix2pix [15] and Cycle GAN [16]—were trained to synthesize PET bone images from the paired CT bone attenuation map images. The discriminator and generator in two GAN networks utilized PatchGAN3D and 3D U-Net respectively. The loss function selected the least squares GAN (LSGAN) loss function [17], and the optimization algorithm was adaptive moment estimation (Adam) optimizer with a learning rate of 0.0001. All images were resized to 128 ×128 ×256 before feeding to models. Other training hyperparameters were set to the batch size of 2, the number of epochs of 1000, and the batch normalization method.

Performance evaluation

The accuracy of the DL-based image synthesis was evaluated using four quantitative metrics, including MAE, MSE, PSNR, and SSIM (Eqs.1–4) [18].

$$SSIM(R,P) = \frac{(2\mu_R\mu_P+c_1)(2\sigma_{RP}+c_2)}{(\mu_R^2+\mu_P^2+c_1)(\sigma_R^2+\sigma_P^2+c_2)}\#(1)$$

$$PSNR(R,P) = 20 \times log_{10}^{\left(\frac{MAX(R)}{\sqrt{MSE(R,P)}}\right)}\#(2)$$

$$MSE(R,P) = \frac{\sum_j^T (R_j-P_j)^2}{T}\#(3)$$

$$MAE(R,P) = \frac{\sum_j^T |R_j-P_j|}{T}\#(4)$$

In Eqs.(1–4), R represents the reference image, and P represents the synthesized image using DL. μ_R and μ_P represent the mean value of the images R and P, and σ_{RP} represents the covariance of R and P. σ_R^2 and σ_P^2 represent the variances of R and P. The constants c_1 and c_2 (c_1=0.01 and c_2=0.02) are used to avoid dividing by numbers close to zero. T represents the total number of voxels. MAX(R) represents the maximum intensity value of R.

In addition, the target-to-background ratio (TBR) values for the test group were calculated on both PET bone images (ground truth) and DL-synthesized PET bone images (Eq. 5).

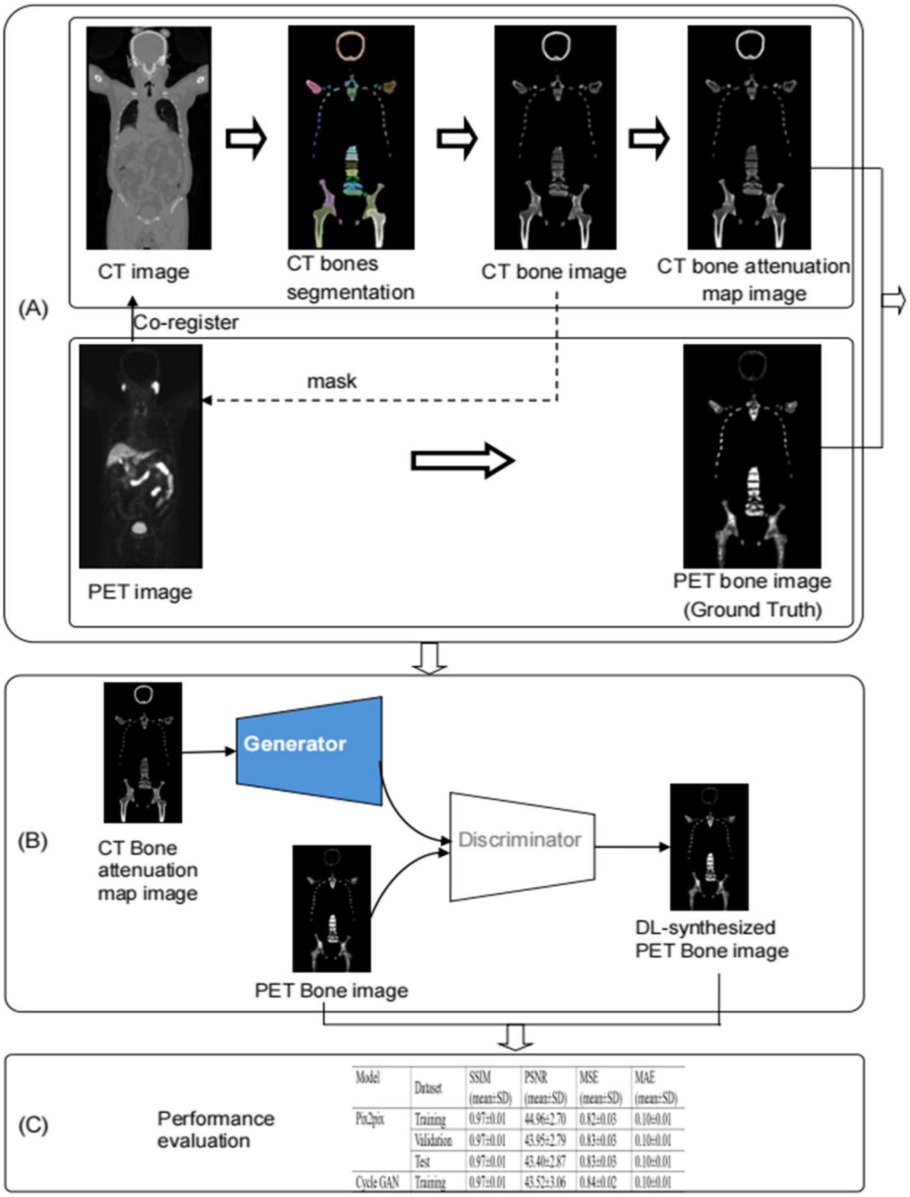

Model	Dataset	SSIM (mean±SD)	PSNR (mean±SD)	MSE (mean±SD)	MAE (mean±SD)
Pix2pix	Training	0.97±0.01	44.96±2.70	0.82±0.03	0.10±0.01
	Validation	0.97±0.01	43.95±2.79	0.83±0.03	0.10±0.01
	Test	0.97±0.01	43.40±2.87	0.83±0.03	0.10±0.01
Cycle GAN	Training	0.97±0.01	43.52±3.06	0.84±0.02	0.10±0.01

Fig. 1 Workflow of the study. **A** PET/CT data preprocessing, segmentation, and bone image construction. **B** GAN models training for image synthesis. **C** Image synthesis performance evaluation

$$TBR = \frac{SUV_{max}\ of\ malignant\ lesion\ ROI}{SUV_{mean}\ of\ contralateral\ normal\ ROI}\#(5)$$

The Pearson correlation coefficient between those two sets of TBR values was computed.

Statistical analysis

All statistical analyses were implemented using Python V3.9 and R software V4.2. Continuous variables were expressed as mean ± standard deviation (SD). The T-test for two groups, and analysis of variance (ANOVA) for more than two groups, were employed for normally distributed continuous variables. The Mann–Whitney U test was used for continuous variables with non-normal distribution. Nominal variables were analyzed using the Fisher's exact test, with results expressed as percentages. A two-tailed p-value <0.05 was considered statistically significant.

Results

There were significant differences in age (t $=-4.48$, $p<0.001$) and lesion size (t $=-10.39$, $p<0.001$) between the benign (29 cases) and malignant (123 cases) groups of patients. The TNM stage distribution in the malignant group included 122 stage N and 77 stage M. The demographic statistical analysis for the training, validation, and test groups is detailed in Table 1. There were no significant differences in demographic distribution among the three groups.

The image synthesis performance of Pix2pix and Cycle GAN models was compared using four quantitative measures—SSIM, PSNR, MSE, and MAE, as shown in Table 2. Two models achieved satisfactory synthesis performance in training, validation, and test groups. In comparison, the Pix2pix model showed better than the Cycle GAN and obtained a higher SSIM value of 0.97 ±0.01, PSNR of 43.40 ±2.87, MSE of 0.83 ±0.03, and MAE of 0.10 ±0.01 on the test groups. The two-tailed t-test results of metrics for the test group indicated no significant differences between the two GAN models ($p < 0.001$ for SSIM, MSE, and MAE, $p < 0.05$ for PSNR).

For 16 patients who had malignant bone metastases in the test group, the TBR values were calculated on PET bone images (ground truth), Pix2pix, and Cycle GAN synthesized PET bone images, respectively. There were no significant differences (all $p < 0.05$) and high Pearson correlation coefficient (all >0.90) for TBRs between ground truth and Pix2pix or Cycle GAN. The TBR distribution among the three sets is depicted in Fig. 2. It indicated that the synthesized PET bone images generated from two GAN models obtained a comparable quality and signal-to-noise ratio to the real PET bone images.

Figure 3 illustrates the [^{18}F]PSMA-1007 WB PET image synthesis results for two patients at stage M who had multiple bone metastases. It clearly shows the bone metastatic lesions of PCa (as pointed out by the yellow arrows) in visual inspection from the synthesized [^{18}F]PSMA-1007 PET image. Two patients presented with multiple lesions in the ribs, vertebrae, pelvis, and femur.

However, it was also observed that the quality of the original [^{18}F]PSMA-1007 PET images directly impacted the quality of the DL ground truth and, as a result, the quality of the synthesized PET bone images. Fig. 4 depicts a case of a synthesized [^{18}F]PSMA-1007 PET bone image with suboptimal quality. In this figure, the original [^{18}F]PSMA-1007 PET image appears excessively smooth, resulting in low resolution of bone structures. As a consequence, the final Pix2pix synthesized PET bone image displays blurry bone structures, leading to overall unsatisfactory quality.

Discussion

This study successfully synthesized [^{18}F]PSMA-1007 PET WB bone images from CT bone images of [^{18}F]PSMA-1007 PET/CT scans, achieving the intended objectives.

Table 1 Demographic statistical analysis for training, validation, and test groups

	Training Group	Validation Group	Test Group	*P*-value
Number of patients	92	41	19	-
Age (mean ± SD, years)	67.37 ± 10.15	69.10 ± 12.76	66.13 ± 11.05	0.564
Weight (mean ± SD, Kg)	74.85 ± 14.39	70.48 ± 8.97	72.97 ± 9.97	0.247
Lesion Size (mean ± SD, mm)	28.00 ± 15.99	30.45 ± 16.02	27.03 ± 13.76	0.694
Number of benign (%)	15 (16.30%)	7 (17.07%)	3 (15.79%)	0.516
Number of malignant (%)	77 (83.70%)	34 (82.93%)	16 (84.21%)	
Number of N0 (%)	16 (17.39%)	8 (19.51%)	6 (31.58%)	0.61
Number of N1 (%)	76 (82.61%)	33 (80.49%)	13 (68.42%)	
Number of M0 (%)	42 (44.65%)	27 (65.85%)	6 (31.37%)	0.287
Number of M1 (%)	50 (54.35%)	14 (34.15%)	13 (68.42%)	

Table 2 Performance comparison of image synthesis GAN models

Model	Dataset	SSIM (mean ± SD)	PSNR (mean ± SD)	MSE (mean ± SD)	MAE (mean ± SD)
Pix2pix	Training	0.97 ± 0.01	44.96 ± 2.70	0.82 ± 0.03	0.10 ± 0.01
	Validation	0.97 ± 0.01	43.95 ± 2.79	0.83 ± 0.03	0.10 ± 0.01
	Test	0.97 ± 0.01	43.40 ± 2.87	0.83 ± 0.03	0.10 ± 0.01
Cycle GAN	Training	0.97 ± 0.01	43.52 ± 3.06	0.84 ± 0.02	0.10 ± 0.01
	Validation	0.96 ± 0.02	41.62 ± 2.81	0.95 ± 0.02	0.20 ± 0.04
	Test	0.95 ± 0.02	41.03 ± 2.70	1.01 ± 0.06	0.24 ± 0.04

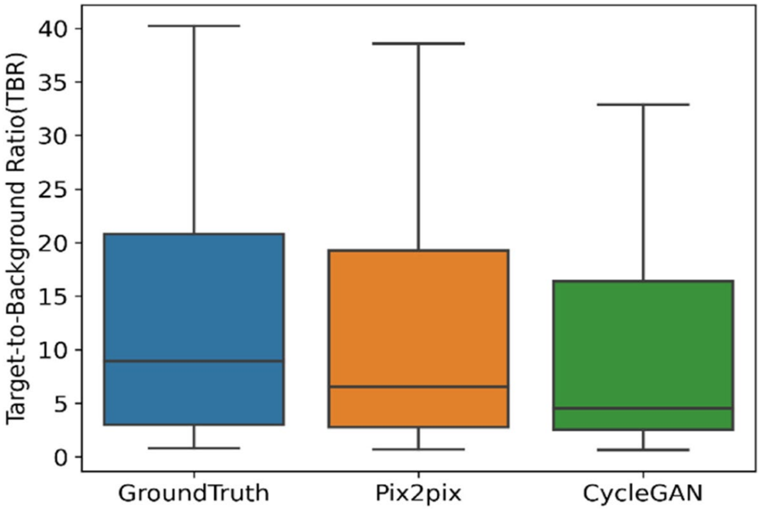

Fig. 2 TBR distribution comparison among the ground truth, Pix2pix, and Cycle GAN synthesized results for patients at stage M in the test group

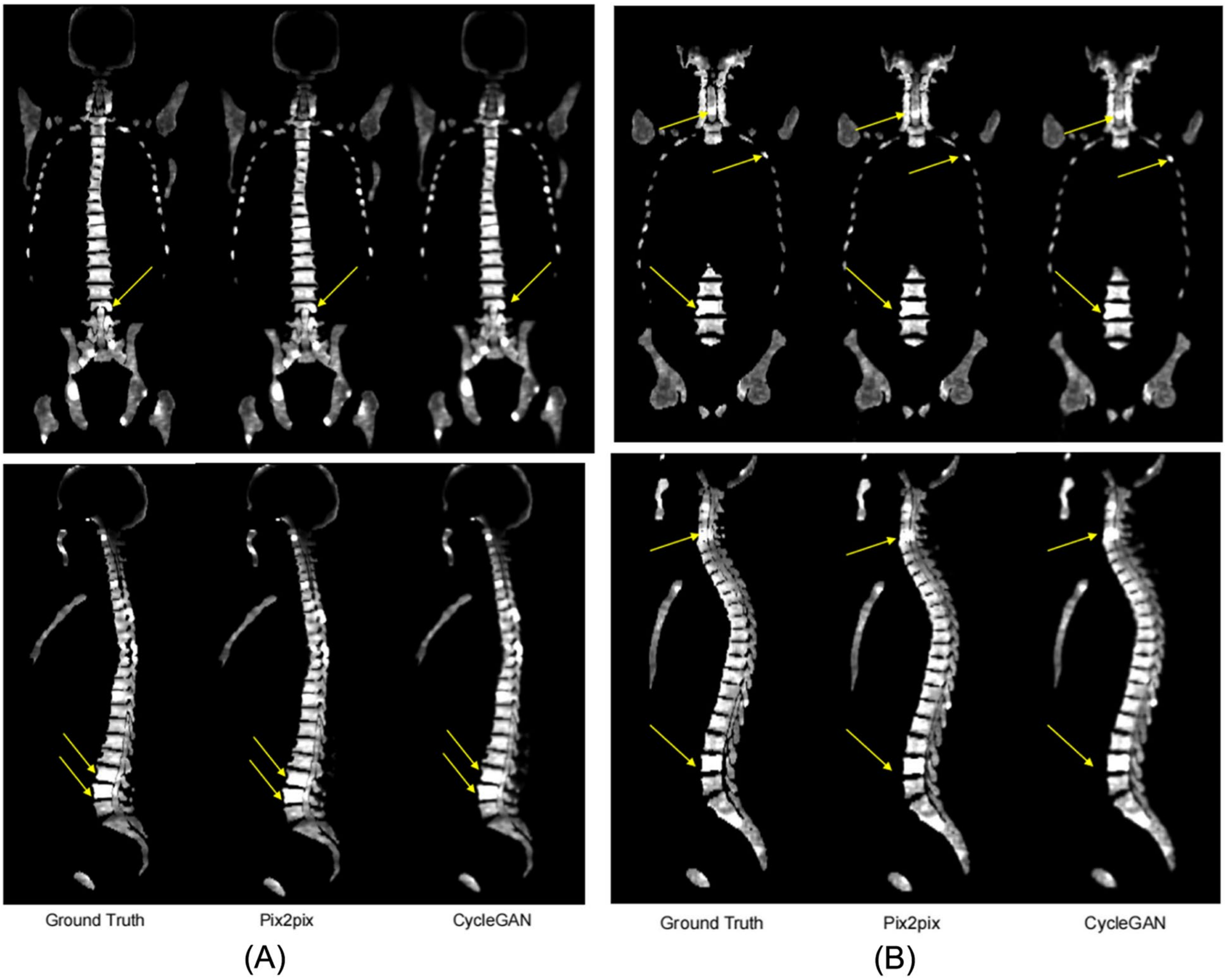

Fig. 3 Coronal and sagittal views of [^{18}F]PSMA-1007 WB PET bone image synthesis results for two patients (**A**) and (**B**) at stage M

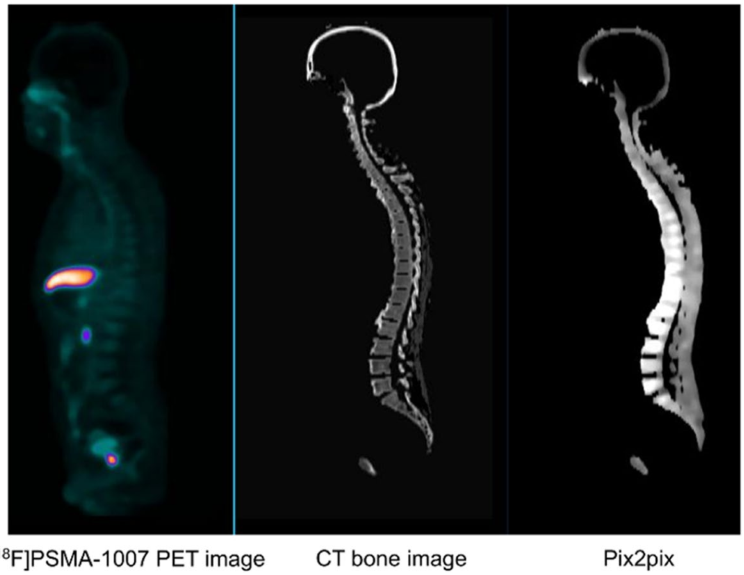

Fig. 4 A case of [^{18}F]PSMA-1007 WB PET bone synthesis image with suboptimal quality at stage M

The method of synthesizing PET images from CT images has been previously reported in the literature [9, 19–22], however, to the best of our knowledge, this is the first time that synthesizing [^{18}F]PSMA-1007 PET images from low-dose CT bone images for detecting bone metastases in PCa is investigated.

Previous studies on PET image synthesis using CT images of PET/CT WB scans have often utilized only partial CT data by clipping partial CT values, not leveraging the full scope of CT image information [9, 19]. In contrast, this study converted CT images from CT Hounsfield Unit (HU) values, typically from −1000 to 1000, to CT attenuation coefficient maps ranging from 0 to 1, thereby preserving all CT image information. This conversion allowed deep neural networks to learn all the features from CT images during model training. Moreover, by using the bone structure extracted from CT and PET images for synthesis, instead of full images, we minimized the impact of [^{18}F]PSMA-1007 PET image uptake in abdominal organs on the detection of skeletal lesions, which in turn improved SSIM, and reduced MSE.

It was observed that both Pix2pix and Cycle GAN models achieved good performance in the image synthesis of this study. The Pix2pix model achieved better quantitative metrics with SSIM, PSNR, MSE, and MAE of 0.97 ±0.01, 44.96 ±2.70, 0.82 ±0.03, and 0.1 ±0.01, respectively. The bone metastasis lesions' TBRs of DL-synthesized images were highly correlated with those of real PET bone images and had no significant differences. The quality of the synthesized images was generally satisfactory visually and quantitatively.

The superior performance of the GAN models can be mainly attributed to the GAN network's architecture, which consists of a generator and a discriminator. This architecture enables the generation of images that closely resemble the true image. As depicted in Fig. 3, the synthesized [^{18}F]PSMA-1007 PET bone image from CT bone image accurately delineates osseous structures and PCa metastases, offering clinically valuable diagnostic information.

Meanwhile, factors impacting the quality of synthesized images were also examined. The primary factor is the quality of the PET images, which is influenced by more factors, including the type of radiopharmaceuticals, scanning speed, motion artifacts, patient physiology, and tumor scintigraphy limitations. Suboptimal [^{18}F]PSMA-1007 images can impact the quality of synthesized images, leading to a low signal-to-noise ratio, as illustrated in Fig. 4. Additionally, the sequential nature of PET/CT scans means that accurate registration between the two modalities is crucial. Registration errors caused by factors such as patient motion, image quality, and registration algorithm can also degrade synthesized image quality.

In general, the results of this study suggest great potential for clinical application. The ability to generate synthetic [^{18}F]PSMA-1007 PET bone images from CT bone images means that CT images in common tracer [^{18}F]FDG PET/CT scans or even routine CT examination alone can provide complementary information for early diagnosis of PCa bone metastases. By doing this, it becomes highly feasible to reduce the number of PET/CT scans which in turn lowers radiation exposure and costs for patients. Thus this process holds crucial clinical value for detecting PCa bone metastases.

Despite the promising results of GANs in image synthesis, it is important to acknowledge their potential pitfalls, such as vanishing gradients, mode collapse, and convergence difficulty [19]. More studies still are needed, preferably utilizing larger datasets and innovative training techniques, to enhance the feasibility of GANs in clinical settings [19].

However, this study has limitations. We utilized a relatively small number of subjects from one center, with only 92 cases in the training group, 41 cases in the validation group, and 19 cases in the test group. Additionally, since less than half of the patients were in stage M and there were substantial differences in the number of metastatic lesions, the clinical diagnosis accuracy has not been fully validated. In addition, the interpretability of the synthesized images by GAN was not visualized and the ablation study was not conducted. Further work will focus on enhancing the generalization of the models by collecting multi-center datasets, conducting in-depth research on their clinical value, and improving network interpretability.

Conclusions

The synthetic [^{18}F]PSMA-1007 PET bone images can be generated from low-dose CT images by utilizing the DL technique with acceptable accuracy. The DL-synthetic [^{18}F]PSMA-1007 PET bone images from CT images can provide complementary information for early detecting bone metastases in patients with PCa.

Abbreviations

Adam	Adaptive moment estimation
ANOVA	Analysis of variance
DL	Deep learning
GAN	Generative adversarial network
HU	Hounsfield Unit
MAE	Mean absolute error
ML	Machine learning
MSE	Mean squared error
PCa	Prostate cancer
PSMA	Prostate-specific membrane antigen
PSNR	Peak signal-to-noise ratio
SD	Standard deviation
SSIM	Structural similarity index metrics
SUV	Standardized uptake values
TBR	Target-to-background ratio
WB	Whole-body

Acknowledgements

We would like to thank the associate editor and the reviewers for their useful feedback that improved this paper.

Authors' contributions

L.C.: conceptualization, methodology, investigation, software, validation, writing and editing, supervision, project administration. Xiaolong Y.: investigation, data curation. Xiaofeng Y.: investigation, data curation. R.N.: software, validation, interpretation of the results. W.Y.: software, validation, interpretation of the results. M.J.: software, validation. H.Z.: software, validation. C.S.: software, validation. Z.D.: software, validation. Xueying Y.: conceptualization, methodology, supervision, project administration. All authors read and approved the final manuscript.

Funding

No funds, grants, or other support were received during the conceptualization, design, data collection, analysis, decision to publish, or preparation of this manuscript.

Data availability

The datasets used and/or analysed during the current study are available from the corresponding author on reasonable request.

Declarations

Ethics approval and consent to participate

This study was performed in line with the principles of the Declaration of Helsinki. Approval was granted by the Ethics Committee of the People's Hospital of Xinjiang Uygur Autonomous Region, China. The committee's reference number was XJS2023021503. Written informed consent was obtained from all patients.

Consent for publication

Not Applicable.

Competing interests

The authors declare no competing interests.

Received: 10 January 2025 Accepted: 9 May 2025

References

1. Berenguer CV, Pereira F, Câmara JS, Pereira JAM. Underlying Features of Prostate Cancer-Statistics, Risk Factors, and Emerging Methods for Its Diagnosis. Curr Oncol. 2023;30(2):2300–21. https://doi.org/10.3390/curroncol30020178.
2. Southern Bone Protection Alliance Prostate Cancer Bone Metastasis Expert Group. Expert consensus on the diagnosis and treatment of bone metastasis in prostate cancer (2023 edition). Chin J Endourol (Electronic Edition). 2023;17(3):201-208.
3. Turpin A, Girard E, Baillet C, et al. Imaging for Metastasis in Prostate Cancer: A Review of the Literature. Front Oncol. 2020;10:55. https://doi.org/10.3389/fonc.2020.00055.
4. Ferrari M, Treglia G. ^{18}F-PSMA-1007 PET in Biochemical Recurrent Prostate Cancer: An Updated Meta-Analysis. Contrast Media Mol Imaging. 2021;2021:3502389. https://doi.org/10.1155/2021/3502389.
5. Saule L, Radzina M, Liepa M, et al. Diagnostic scope of ^{18}F-PSMA-1007 PET/CT: comparison with multiparametric MRI and bone scintigraphy for the assessment of early prostate cancer recurrence. Am J Nucl Med Mol Imaging. 2021;11(5):395–405.
6. Mena E, Black PC, Rais-Bahrami S, Gorin M, Allaf M, Choyke P. Novel PET imaging methods for prostate cancer. World J Urol. 2021;39(3):687–99. https://doi.org/10.1007/s00345-020-03344-3.
7. Xing Zhou, YingChun Li, et al. Intra-Individual Comparison of ^{18}F-PSMA-1007 and ^{18}F-FDG PET/CT in the Evaluation of Patients With Prostate Cancer. Front Oncol. 2021. https://doi.org/10.3389/fonc.2020.585213.
8. Dayarathna Sanuwani, Islam Kh Tohidul, Uribe Sergio, Yang Guang, Hayat Munawar, Chen Zhaolin. Deep learning based synthesis of MRI, CT and PET: Review and analysis. Med Image Anal. 2024;92:103046. https://doi.org/10.1016/j.media.2023.103046.
9. Salehjahromi M, Karpinets TV, Sujit SJ, Qayati M, Chen P, Aminu M, Saad MB, et al. Synthetic PET from CT improves diagnosis and prognosis for lung cancer: Proof of concept. Cell Rep Med. 2024;5(3): 101463. https://doi.org/10.1016/j.xcrm.2024.101463.

10. Sanaat A, Boccalini C, et al. A deep learning model for generating [^{18}F] FDG PET Images fromearly-phase [^{18}F]Florbetapir and[^{18}F]Flutemetamol PET images. Eur J Nucl Med Mol Imaging. 2024;51:3518–31. https://doi.org/10.1007/s00259-024-06755-1.
11. Zamani-Siahkali Nazanin, Mirshahvalad Seyed Ali, et al. SPECT/CT, PET/CT, and PET/MRI for Response Assessment of Bone Metastases. Semin Nucl Med. 2024;54(3):356–370.
12. Klein S, Staring M, Murphy K, Viergever MA, Pluim JP. Elastix: a toolbox for intensity-based medical image registration. IEEE Trans Med Imaging. 2010;29(1):196–205. https://doi.org/10.1109/tmi.2009.2035616.
13. Wasserthal Jakob, Breit Hanns-Christian, Meyer Manfred T, et al. TotalSegmentator: Robust Segmentation of 104 Anatomic Structures in CT Images. Radiol Artif Intell. 2023;5(5):e230024. https://doi.org/10.1148/ryai.230024.
14. Abella M, Alessio AM, Mankoff DA, et al. Accuracy of CT-based attenuation correction in PET/CT bone imaging. Phys Med Biol. 2012;57(9):2477–90. https://doi.org/10.1088/0031-9155/57/9/2477.
15. Isola Phillip, Zhu Jun-Yan, Zhou Tinghui, Efros Alexei A. Image-to-Image Translation with Conditional Adversarial Networks. 2017 IEEE International Conference on Computer Vision and Pattern Recognition (CVPR). https://doi.org/10.48550/arXiv.1611.07004.
16. Jun-Yan Zhu, Taesung Park, Phillip Isola, Alexei A. Efros. Unpaired image-to-image translation using cycle-consistent adversarial networks. 2017 IEEE International Conference on Computer Vision (ICCV). Venice: 2017. pp. 2242-2251. https://doi.org/10.1109/ICCV.2017.244.
17. Xudong Mao, Qing Li, et al. Least Squares Generative Adversarial Networks. 2017 IEEE International Conference on Computer Vision (ICCV). https://doi.org/10.48550/arXiv.1611.04076.
18. Sara U, Akter M, Uddin MS. Image Quality Assessment through FSIM, SSIM, MSE, and PSNR-a Comparative Study. Journal of Computer and Communications. 2019;7(3):8–18.
19. Wang T, Lei Y, Fu Y, Wynne JF, Curran WJ, Liu T, Yang X. A review on medical imaging synthesis using deep learning and its clinical applications. J Appl Clin Med Phys. 2021;22(1):11–36. https://doi.org/10.1002/acm2.13121.
20. Pianou NK, Stavrou PZ, Vlontzou E, Rondogianni P, Exarhos DN, Datseris IE. More advantages in detecting bone and soft tissue metastases from prostate cancer using ^{18}F-PSMA PET/CT. Hell J Nucl Med. 2019;22(1):6–9. https://doi.org/10.1967/s002449910952.
21. Lindgren Belal S, Frantz S, Minarik D, et al. Applications of Artificial Intelligence in PSMA PET/CT for Prostate Cancer Imaging. Semin Nucl Med. 2024;54(1):141–9. https://doi.org/10.1053/j.semnuclmed.2023.06.001.
22. Janssen J, Noordzij W, Velleman T, et al. ^{18}F-PSMA-1007 uptake in prostate cancer patients. Ther Adv Med Oncol. 2023;15:17588359231179312. https://doi.org/10.1177/17588359231179311.

Publisher’s Note